NANOPARTICLES

Production of amorphous nanoparticles by supersonic spray-drying with a microfluidic nebulator

Esther Amstad,[1,2] Manesh Gopinadhan,[3] Christian Holtze,[4] Chinedum O. Osuji,[3] Michael P. Brenner,[1] Frans Spaepen,[1] David A. Weitz[1,5]*

Amorphous nanoparticles (a-NPs) have physicochemical properties distinctly different from those of the corresponding bulk crystals; for example, their solubility is much higher. However, many materials have a high propensity to crystallize and are difficult to formulate in an amorphous structure without stabilizers. We fabricated a microfluidic nebulator that can produce amorphous NPs from a wide range of materials, even including pure table salt (NaCl). By using supersonic air flow, the nebulator produces drops that are so small that they dry before crystal nuclei can form. The small size of the resulting spray-dried a-NPs limits the probability of crystal nucleation in any given particle during storage. The kinetic stability of the a-NPs—on the order of months—is advantageous for hydrophobic drug molecules.

The properties of nanoparticles (NPs) can differ greatly from those of their bulk counterparts, and for materials that are normally crystalline, even greater differences can be achieved by making amorphous NPs (a-NPs). For example, the solubility of a given material can be greatly enhanced even when its crystalline counterpart is very poorly soluble (*1*). Many materials have a very high propensity to crystallize, so it is challenging to produce amorphous structures in widely applicable ways. Inorganic materials that can be evaporated into the gas phase can form a-NPs via aggregation into amorphous clusters (*2*, *3*). In addition, some metals can be processed into a-NPs by rapidly cooling drops composed of melts (*4*, *5*). However, the majority of inorganic materials cannot be processed in this manner, and even fewer organic materials can be so processed. Instead, the most common route to process organic materials into NPs is through precipitation from solution (*6*–*9*).

For materials with a high propensity to crystallize, crystallization is typically much faster than termination of the precipitation reaction, and the resultant NPs are crystalline. a-NP production thus requires the addition of crystallization inhibitors (*10*), which must be carefully chosen for each crystallization-prone material. In some specific cases, the solution can be rapidly cooled to freezing, followed by lyophilization of the resulting particles (*11*, *12*). Alternatively, the solution can be formed into drops through spray-drying (*13*–*15*). In this case, NPs start to form when the solute concentration exceeds its saturation concentration (*16*, *17*). However, the rate of crystallization is typically still much faster than the rate of NP growth, and crystallization inhibitors are still required to create a-NPs. Nearly half of all drug compounds are hydrophobic (*1*), and formulating them as a-NPs would increase their bioavailability (*18*), solubility (*1*), and dissolution rates (*19*).

We show how to produce a-NPs from a range of materials without the use of any crystallization inhibitors. Our process uses a microfluidic

[1]School of Engineering and Applied Sciences, Harvard University, Cambridge, MA, USA. [2]Institute of Materials, Ecole Polytechnique Fédérale de Lausanne, Lausanne, Switzerland. [3]Department of Chemical and Environmental Engineering, Yale University, New Haven, CT, USA. [4]BASF SE, D-67056 Ludwigshafen, Germany. [5]Department of Physics, Harvard University, Cambridge, MA, USA.
*Corresponding author. E-mail: weitz@seas.harvard.edu

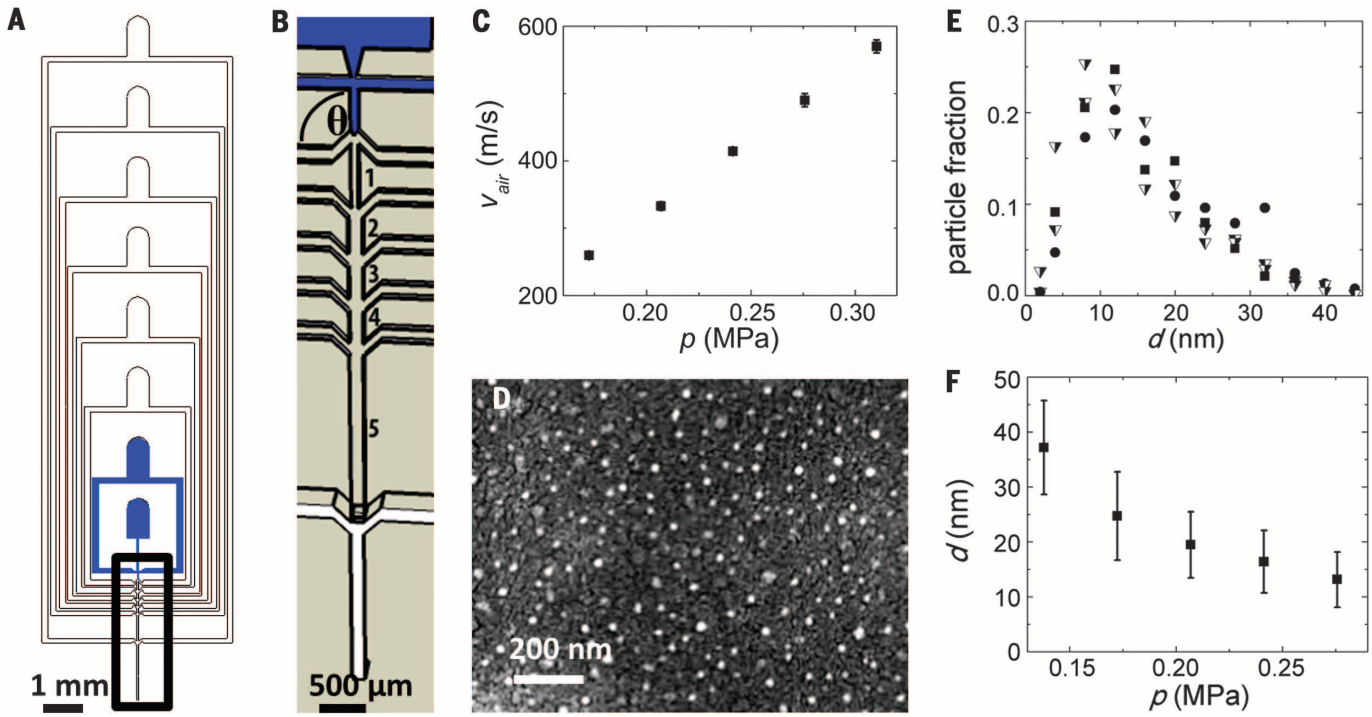

Fig. 1. The microfluidic nebulator. (**A** and **B**) Overview (A) and close-up (B) of a microfluidic nebulator. Liquids are injected through blue inlets; air is introduced through white inlets. (**C**) Air velocity at outlet as a function of pressure applied to all air inlets; error bars indicate the variance of air velocities measured in different devices. (**D**) SEM micrograph of spray-dried fenofibrate NPs. (**E**) Size distribution of fenofibrate (■), clotrimazole (●), danazol (▼), and estradiol (▽) NPs. (**F**) Size of fenofibrate NPs as a function of air pressure; error bars indicate the size distribution of NPs produced in different batches.

nebulator—a spray drier that enables supersonic air speeds to be achieved at moderate pressures. Liquids are nebulized into very small drops whose dimensions limit the size of the resultant spray-dried NPs. The very rapid evaporation of the solvent creates a kinetically arrested glass in the evaporating drop and prevents formation of crystal nuclei. The nebulator can produce a-NPs from both organic and inorganic materials, including materials with a very high propensity to crystallize, such as table salt (NaCl). The small size of these a-NPs (<15 nm) results in exceptionally high stability against crystallization, with most a-NPs maintaining that state under ambient conditions and at room temperature for at least 7 months.

We fabricated the nebulator from poly(dimethyl siloxane) (PDMS) using soft lithography (*20*). A main fluid-inlet channel is intersected by a pair of inlets for an additional fluid so that two fluid streams can mix if it is necessary to initiate chemical reactions prior to drop formation. The nebulator also has six air inlets (Fig. 1, A and B). The last junction is three-dimensional (3D), with a small inlet opening into a channel of larger dimensions (Fig. 1B) (*21*). We sliced the end of the main channel to make the final outlet (*15*). The same pressure was applied to each of the air inlets; the device can reliably sustain inlet pressures up to 0.28 MPa (~2.8 atm) before the PDMS bonding fails. The velocity of the air at the outlet scales with the inlet pressure (Fig. 1C).

To demonstrate the operation of the nebulator, we used a generic hydrophobic organic drug, fenofibrate, which has a high propensity for crystallization. We dissolved fenofibrate in ethanol (5 mg/ml) and injected this solution into the first fluid inlet at a flow rate of 1 ml/hour. We inverted the direction of the first pair of air inlets to inject the air in the opposite direction to the ethanol flow (Fig. 1B). Because ethanol strongly wets the channel walls, thin homogeneous ethanol films were formed and flowed along the four channel walls. These films were detached from the walls at the 3D junction, where they broke into very small drops whose diameter must be similar to the film thickness. The drops began to dry through evaporation as they exited the device, forming NPs that were collected on a substrate placed 10 cm from the outlet.

Remarkably, NPs with an average diameter of 14 nm were produced with an inlet pressure of 0.28 MPa (Fig. 1D and fig. S1). Drug particles produced with commercially available spray-dry instruments typically have diameters greater than 350 nm (*14*, *22*–*26*). We also produced NPs from other hydrophobic drugs, including clotrimazole, estradiol, and danazol, with similar size distributions (Fig. 1E). The thickness of the liquid film produced in the nebulator scaled inversely with applied air pressure, so the NP size decreased roughly inversely with increasing air pressure (Fig. 1F). This relation suggests that NPs as small as 1 nm could be produced with an inlet air pressure of 0.54 MPa.

The smallest-sized fenofibrate NPs (14 nm) were always amorphous, as indicated by the lack of any lattice plane in the high-resolution transmission electron microscope (HRTEM) image and the absence of distinct diffraction peaks in its Fourier transform (Fig. 2A), as well as the absence of any peaks in x-ray diffraction (XRD) (Fig. 2B, top trace). By contrast, crystalline NPs (c-NPs) formed when spray-dried in the presence of Pluronics F127, which acted as a heterogeneous nucleant. These c-NPs had clear diffraction peaks (fig. S2, top trace) (*27*), which also validates the use of XRD to determine the structure of our spray-dried NPs. Fenofibrate has a glass transition temperature T_g of –20°C (*28*) and a melting temperature T_m of 80°C (*29*), so fenofibrate a-NPs must be undercooled liquids at room temperature. Similar amorphous structures were observed for small NPs formed from all other drugs tested (figs. S3 and S4); however, the others are glasses, as they all have T_g above room temperature.

We argue that a-NPs form as a result of this production route. Fenofibrate crystals can nucleate as soon as the solvent in the drop has evaporated sufficiently for the solute concentration to exceed its saturation value. Once a crystal nucleus is formed, crystal growth should transform the entire a-NP. Thus, formation of a-NPs can occur only if crystal nucleation is inhibited. We calculated the number of crystal nuclei that form in a drop as it evaporates, N, using classical nucleation theory under isothermal conditions (*17*, *27*). As the solvent evaporates, the solute concentration becomes very high and the resultant nucleation rate is large. Even drops as small as 100 nm, which produce the 14-nm NPs, should yield c-NPs.

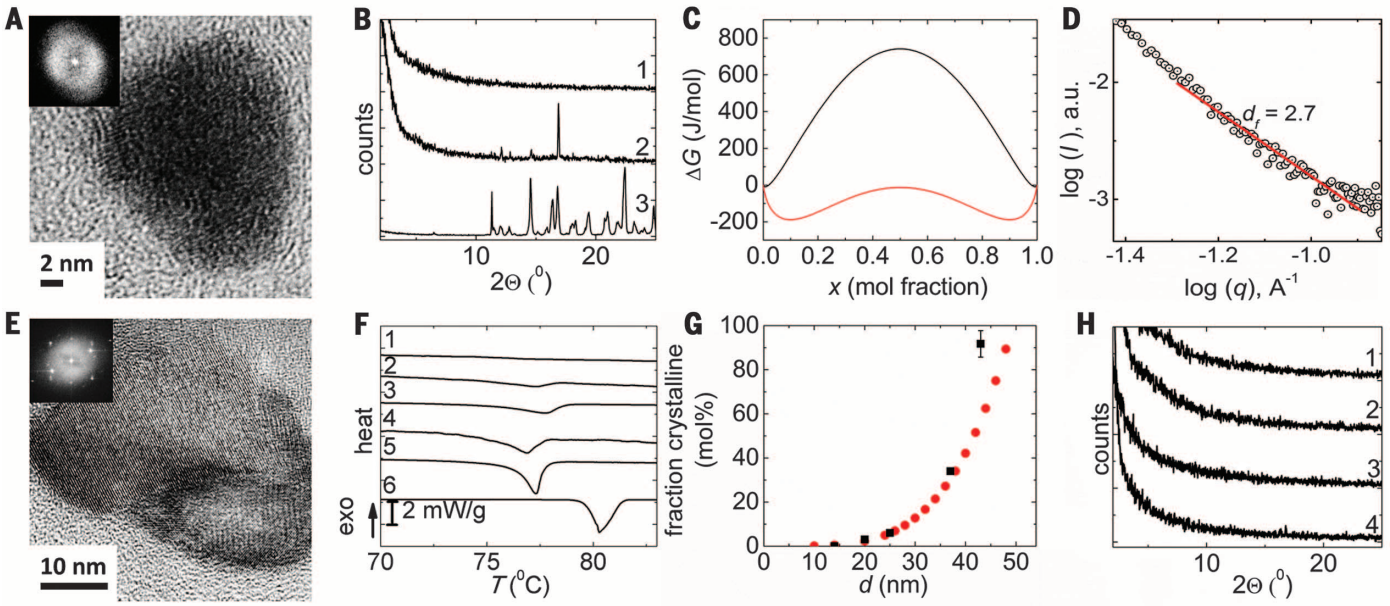

Fig. 2. Structure of spray-dried fenofibrate NPs. (**A**) HRTEM micrograph of fenofibrate spray-dried at 0.28 MPa, with the Fourier transform in the inset. (**B**) XRD spectra of fenofibrate spray-dried with inlet air pressures of (1) 0.28 MPa and (2) 0.14 MPa; crystalline fenofibrate (3) is shown as a reference. (**C**) Free energy of formation of fenofibrate-ethanol solution, ΔG, at room temperature (red curve) and –70°C (black curve). (**D**) SAXS data of fenofibrate NPs with the power-law fit (solid line). (**E**) TEM image of fenofibrate spray-dried at 0.14 MPa, with the Fourier transformation in the inset. (**F**) DSC traces of fenofibrate NPs produced at (1) 0.28 MPa, (2) 0.21 MPa, (3) 0.17 MPa, (4) 0.14 MPa, and (5) 0.12 MPa; crystalline fenofibrate (6) is shown as a reference. (**G**) Fraction of c-NPs measured by integrating the melting peaks of the DSC traces (■) and calculated (●) as a function of their diameter; the error bars indicate the variance between particles produced in different batches. (**H**) XRD traces of fenofibrate NPs stored at (1) room temperature for 7 months, (2) 40°C for 6 months, (3) 65°C for 2 months, and (4) 65°C for 3 months.

The calculation of the nucleation rate assumes a homogeneous distribution of fenofibrate in the evaporating solvent.

However, if there is an attractive interaction between the solute molecules, they can undergo spinodal decomposition more rapidly than crystals nucleate, leading to high spatial heterogeneity. To determine whether there is an attractive interaction between fenofibrate molecules, we compute the difference in the Gibbs free energy between the individual components and the solution, ΔG, as a function of the solution composition (*27*). It has two minima, implying that this solution phase separates, as indicated by the red curve in Fig. 2C. The low concentration in the solute-poor phase will decrease the rate of crystal nucleation. The high concentration in the solute-rich phase will increase the rate of crystallization, but the viscosity will also increase, thus also reducing the rate of crystal nucleation.

We estimate that the rate of crystallization at room temperature would still result in c-NPs. However, the drop is also subjected to evaporative cooling: It decreases the drop temperature to a new steady-state value, determined by the balance of evaporative cooling and heat transferred from the air to the drop. Because of the rapid air flow, the boundary layers at the surface of the drop for both molecular transport and heat diffusion are very thin, resulting in both rapid evaporation and rapid heat transport. We estimate the new temperature to be T = –70°C (*27*). At this temperature, the solute-rich phase contains only 1 mol% of solvent, as shown by the black curve in Fig. 2C. Hence, the viscosity of the solute-rich phase is further increased by the increased solute concentration and the reduced temperature; this decreases the mobility of fenofibrate molecules and thus the rate of crystal nucleation.

Similarly, the reduced temperature decreases the nucleation rate in the solute-poor phase by reducing the solute mobility, but to a smaller extent. If the drop is sufficiently small, it will evaporate faster than crystal nuclei can form; thus, the NPs will remain amorphous. We postulate that the origin of the amorphous structure is kinetic arrest of the solute molecules into a glassy state. This mechanism, which involves a rapid increase in solute concentration accompanied by a decrease in temperature, is fundamentally different from the formation of conventional glasses, where the formation of crystal nuclei is kinetically suppressed only through a fast reduction in temperature. Intriguingly, the glass formation inside drops is similar to that observed for attractive colloidal particles that undergo kinetic arrest (*30–32*).

To test our postulate, we investigated the morphology of the NPs. The structure of a kinetically arrested glassy phase formed by spinodal decomposition should be highly tenuous, and remnants of this irregularity may persist even after the drop fully dries. We used small-angle x-ray scattering (SAXS) to investigate the structure of 14-nm fenofibrate NPs at scattering vectors, q, corresponding to length scales smaller than the particle size. We observe a power-law dependence of the scattered intensity, $I(q) \propto q^{d_f}$, consistent with a fractal structure having a fractal dimension d_f = 2.7 (Fig. 2D). Thus, the structure of the NPs is highly irregular, consistent with formation from spinodal decomposition (*33*).

Further validation of our postulate comes from the formation of larger drops, which take longer to dry and hence allow more time for nuclei to form. When we seeded a small crystal of fenofibrate in a supercooled liquid of pure fenofibrate, formed by spray-drying, it grew very rapidly. Thus, even if only a single crystal nucleation event occurred inside an evaporating drop, the entire particle would crystallize upon warming. Indeed, some 40-nm-diameter NPs were fully crystalline, as shown by HRTEM (Fig. 2E), by XRD (Fig. 2B, middle trace), and by the appearance of a melting peak measured with differential scanning calorimetry (DSC) (Fig. 2F, second thermogram), albeit at a lower temperature than observed for bulk melting.

To quantify the percentage of c-NPs, we determined the crystalline fraction as a function of NP size by integrating the area of the DSC melting peaks shown in Fig. 2F. The fraction of c-NPs increased with increasing NP size (Fig. 2G, black squares). For comparison, we predicted the crystalline fraction by calculating N as a function of NP size and found excellent agreement with experiment (Fig. 2G).

One of the major obstacles to the use of the amorphous structure for drugs is the high propensity toward crystallization during storage (*34*). Surprisingly, although the 14-nm fenofibrate a-NPs are undercooled liquids that are either deposited as monolayers or coated with a polymer to prevent aggregation, they remained amorphous even when stored for 7 months at room temperature under ambient conditions, as shown by XRD (Fig. 2H, first curve), and for at least 6 months if stored under ambient conditions at 40°C (Fig. 2H, second curve). Moreover, fenofibrate NPs remained amorphous for up to 2 months if stored even at 65°C (Fig. 2H, third curve) and only began to crystallize after 3 months, as indicated by the small XRD diffraction peaks at 2θ = 16.3° and 16.8° (Fig. 2H, fourth curve). We attribute this exceptionally high stability to the small NP size. If compartmentalized into many small NPs, crystal growth is kinetically restricted, as a large number of nuclei must form to fully crystallize the sample.

We also used the microfluidic nebulator to formulate inorganic a-NPs. For example, we formed $CaCO_3$ NPs exploiting the two liquid inlets to co-inject one aqueous solution containing 5 mM $CaCl_2$ and another containing 5 mM Na_2CO_3. As soon as the two solutions were combined, nuclei of $CaCO_3$ could start to precipitate from the supersaturated solution. Water does not wet the PDMS walls. Nevertheless, we could use the same device design to operate the nebulator in the dripping regime, where drops of water are formed at the first inlet. The air from the first inlet must reverse its flow direction to enter the main

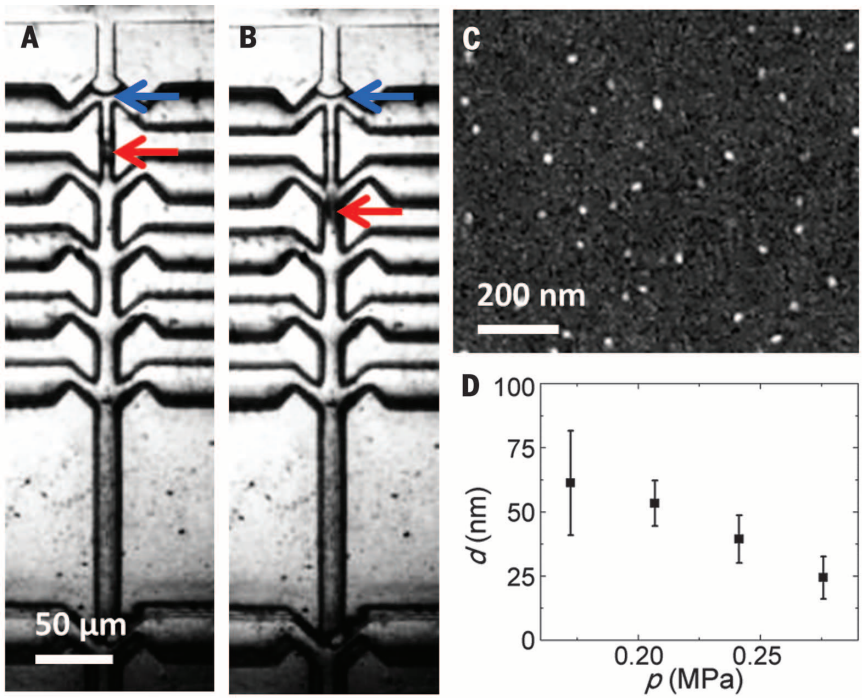

Fig. 3. Operation of the nebulator using a nonwetting fluid. (**A** and **B**) Optical micrographs of the nebulator operated with water, taken 120 µs (A) and 280 µs (B) after the drop pinched off. Red arrows point to the drops, blue arrows to the stagnation point of the air velocity v_x. (**C**) SEM image of spray-dried $CaCO_3$ NPs. (**D**) Size of $CaCO_3$ NPs as function of the air pressure; error bars indicate the size distribution of NPs produced in different batches.

channel. This configuration created a stagnation point where the component of the air velocity in the direction of the main channel, v_x, equals zero; this produced a stationary instability and dripping (Fig. 3, A and B, and movie S1). The size of these drops was similar to the channel dimension. Thus, the distance between the drop surface and the channel wall, l, was small, and the local shear stress, $\tau = \mu(dv/l)$, was very high; here, μ is the viscosity of air. This large shear stress overcame the Laplace pressure of the primary drop, breaking it into much smaller drops whose radius r was determined by the balance of the shear stress and the Laplace pressure $\mu(dv/l) = \gamma/r$; here, γ is the surface tension.

To estimate a lower limit for τ, we determined an upper limit of l using microscope images and determined dv by measuring the velocity at the outlet and calculating the velocity profile inside the device (*27*). The resultant shear stress was very large and produced drops as small as 400 nm in diameter, which would lead to 30-nm NPs. Consistent with this calculation, the size of the spray-dried $CaCO_3$ NPs measured from scanning electron microscopy (SEM) images is 20 nm (Fig. 3C). The NP size increased with decreasing pressure applied to the air inlet (Fig. 3D), in accord with our calculations. These $CaCO_3$ NPs were chemically homogeneous, as determined by electron-dispersive spectroscopy (EDS) (fig. S5). For NPs with diameters less than 20 nm, there was no evidence of crystallinity revealed by HRTEM (Fig. 4A). By contrast, NPs exceeding 40 nm contained multiple crystal nuclei embedded in an amorphous matrix. In this case, crystal growth was much slower than for fenofibrate, and we could visualize intermediate stages of the crystallization where crystalline regions coexist with amorphous ones (Fig. 4B). If the NPs were sufficiently small, the nebulator could make a-NPs from inorganic materials with a greater propensity to crystallize, such as $BaSO_4$ and iron oxide, as shown in the HRTEM images in fig. S6, A and B, respectively.

A common material with a very high propensity to crystallize is table salt, NaCl. Amorphous NaCl has not been reported, although small amorphous clusters have been predicted by molecular dynamics simulations (*35*). Remarkably, the nebulator could produce a-NPs of NaCl if their diameter was below 15 nm, as indicated in HRTEM images and the corresponding Fourier transform in Fig. 4C and the bottom XRD spectrum in Fig. 4E. Moreover, x-ray photoelectron spectroscopy (XPS) showed that the binding energy of the Na 1s peak was shifted toward lower energies, indicating that the nearest neighbors of the Na ions are farther apart, or on average less electronegative, than the nearest neighbors of Na contained in the NaCl structure (Fig. 4F, bottom spectrum). Moreover, the Cl 1s peak was broadened, indicating that the distances of the nearest neighbors of the Cl ions vary (fig. S7, bottom spectrum). Larger NaCl NPs were crystalline, as indicated by the HRTEM micrograph in Fig. 4D, the (220) reflection at $2\theta = 45.5°$ in the middle XRD trace in Fig. 4E, and the unchanged binding energies of the Na 1s and Cl 1s peaks measured with XPS and shown respectively in the second spectra in Fig. 4F and fig. S7. The only materials with which we have been unable to form a-NPs are Au, Ag, and Pt.

The production rate of a single nebulizer is limited by its scale; thus, to make more useful quantities of material, the nebulators must be scaled up in number. We operated three nebulators in parallel with common inlets and increased throughput to 15 mg of material per hour, which is sufficient for laboratory-scale tests such as drug bioavailability. Hydrodynamic coupling between devices did not compromise their performance when operated in parallel, so further scale-up in the number of coupled nebulators should be feasible.

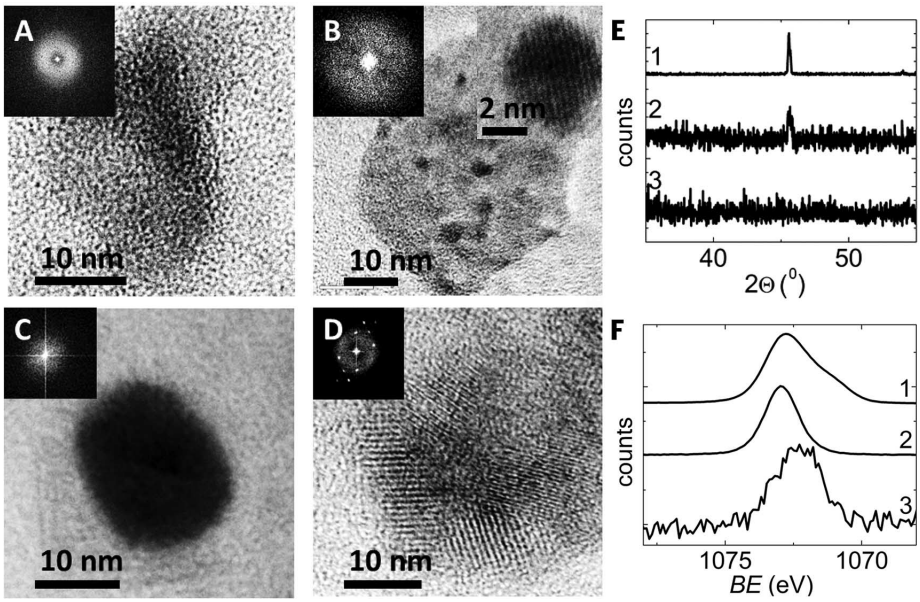

Fig. 4. Structure of spray-dried inorganic NPs. (**A** and **B**) HRTEM images, with Fourier transform insets, of $CaCO_3$ NPs produced at air inlet pressures of 0.28 MPa (A) and 0.21 MPa (B). The inset in (B) is a HRTEM of one of the dark spots shown in the main image, showing small amounts of crystal formation for this NP size. (**C** and **D**) HRTEM images of NaCl NPs spray-dried from aqueous solutions initially containing 4 mM NaCl (C) and 40 mM NaCl (D); the insets show their Fourier transforms. (**E**) XRD traces of (1) c-NaCl produced by slowly evaporating an aqueous solution containing 40 mM NaCl, (2) spray-dried NaCl NPs produced from a solution containing 40 mM NaCl, and (3) spray-dried NaCl NPs produced from a solution containing 4 mM NaCl. (**F**) XPS spectra of the Na 1s peak of (1) crystalline reference NaCl, (2) NaCl NPs spray-dried from a solution initially containing 40 mM NaCl, and (3) NaCl NPs spray-dried from a solution initially containing 4 mM NaCl.

REFERENCES AND NOTES

1. Y. Kawabata, K. Wada, M. Nakatani, S. Yamada, S. Onoue, *Int. J. Pharm.* **420**, 1–10 (2011).
2. A. H. Tavakoli *et al.*, *J. Phys. Chem. C* **117**, 17123–17130 (2013).
3. L. Landström, J. Kokavecz, J. Lu, P. Heszler, *J. Appl. Phys.* **95**, 4408 (2004).
4. Y. W. Kim, H. M. Lin, T. F. Kelly, *Acta Metall.* **37**, 247–255 (1989).
5. A. L. Greer, *Nat. Mater.* **14**, 542–546 (2015).
6. P. Guo, T. M. Hsu, Y. Zhao, C. R. Martin, R. N. Zare, *Nanomedicine* **8**, 333–341 (2013).
7. L. Yu, C. Li, Y. Le, J.-F. Chen, H. Zou, *Mater. Chem. Phys.* **130**, 361–366 (2011).
8. W.-Z. Zhu *et al.*, *Int. J. Pharm.* **395**, 260–265 (2010).
9. R. S. Dhumal, S. V. Biradar, S. Yamamura, A. R. Paradkar, P. York, *Eur. J. Pharm. Biopharm.* **70**, 109–115 (2008).
10. M. E. Matteucci, M. A. Hotze, K. P. Johnston, R. O. Williams 3rd, *Langmuir* **22**, 8951–8959 (2006).
11. W. Yang *et al.*, *Int. J. Pharm.* **361**, 177–188 (2008).
12. K. A. Overhoff *et al.*, *Eur. J. Pharm. Biopharm.* **65**, 57–67 (2007).
13. J.-S. Kim *et al.*, *Int. J. Pharm.* **359**, 211–219 (2008).
14. S. N. Harsha *et al.*, *Drug Design Dev. Ther.* **9**, 273–282 (2015).
15. J. Thiele *et al.*, *Lab Chip* **11**, 2362–2368 (2011).
16. M. E. Matteucci *et al.*, *Mol. Pharm.* **4**, 782–793 (2007).
17. K. F. Kelton, A. L. Greer, *Nucleation in Condensed Matter Applications in Materials and Biology* (Elsevier, New York, 2010).
18. B. C. Hancock, M. Parks, *Pharm. Res.* **17**, 397–404 (2000).
19. F. Kesisoglou, S. Panmai, Y. Wu, *Adv. Drug Deliv. Rev.* **59**, 631–644 (2007).
20. Y. N. Xia, G. M. Whitesides, *Annu. Rev. Mater. Sci.* **28**, 153–184 (1998).
21. A. Rotem, A. R. Abate, A. S. Utada, V. Van Steijn, D. A. Weitz, *Lab Chip* **12**, 4263–4268 (2012).
22. S. Harsha, *Drug Design Dev. Ther.* **7**, 1027–1033 (2013).
23. C. Arpagaus, *Dry. Technol.* **30**, 1113–1121 (2012).
24. K. Bürki, I. Jeon, C. Arpagaus, G. Betz, *Int. J. Pharm.* **408**, 248–256 (2011).
25. X. Li, N. Anton, C. Arpagaus, F. Belleteix, T. F. Vandamme, *J. Control. Release* **147**, 304–310 (2010).
26. V. Martena, R. Censi, E. Hoti, L. Malaj, P. Di Martino, *J. Nanopart. Res.* **14**, 934 (2012).
27. See supplementary materials on *Science* Online.
28. Y. C. Ng, Z. Yang, W. J. McAuley, S. Qi, *Eur. J. Pharm. Biopharm.* **84**, 555–565 (2013).
29. D. Law *et al.*, *J. Pharm. Sci.* **92**, 505–515 (2003).
30. P. J. Lu *et al.*, *Nature* **453**, 499–503 (2008).

31. V. Trappe, V. Prasad, L. Cipelletti, P. N. Segre, D. A. Weitz, *Nature* **411**, 772–775 (2001).
32. A. J. Liu, S. R. Nagel, *Nature* **396**, 21–22 (1998).
33. J. H. Page *et al.*, *Phys. Rev. E* **52**, 2763–2777 (1995).
34. R. Laitinen, K. Löbmann, C. J. Strachan, H. Grohganz, T. Rades, *Int. J. Pharm.* **453**, 65–79 (2013).
35. I. G. Nahtigal, I. M. Svishchev, *J. Phys. Chem. B* **113**, 14681–14688 (2009).

ACKNOWLEDGMENTS

We acknowledge support from BASF SE, NSF grants DMR-1310266 and DMS-1411694, and Harvard MRSEC grant DMR-1420570. M.P.B. is an investigator of the Simons Foundation. Part of this work was performed at the Center for Nanoscale Systems (CNS), a member of the National Nanotechnology Infrastructure Network, supported by NSF award no. ECS-0335765. CNS is part of Harvard University. We thank D. C. Bell for acquiring the EDS images and L. R. Arriaga and D. M. Aubrecht for helpful discussions. Patent applications have been filed to cover the nebulator device (PCT/US2013/060522) and the production of a-NPs (PCT/US2014/062785). Additional data discussed in the main text are available in the supplementary materials. E.A. conducted the experiments; M.G. performed the SAXS experiments and analysis; E.A., F.S., and D.A.W. did the calculations and wrote the paper; and all the authors contributed to the design and analysis of the experiments.

SUPPLEMENTARY MATERIALS

www.sciencemag.org/content/349/6251/956/suppl/DC1
Materials and Methods
Supplementary Text
Figs. S1 to S8
Movie S1
References (*36*, *37*)

5 July 2015; accepted 31 July 2015
10.1126/science.aac9582

ORGANIC CHEMISTRY

Iron-catalyzed intermolecular [2+2] cycloadditions of unactivated alkenes

Jordan M. Hoyt, Valerie A. Schmidt, Aaron M. Tondreau, Paul J. Chirik*

Cycloadditions, such as the [4+2] Diels-Alder reaction to form six-membered rings, are among the most powerful and widely used methods in synthetic chemistry. The analogous [2+2] alkene cycloaddition to synthesize cyclobutanes is kinetically accessible by photochemical methods, but the substrate scope and functional group tolerance are limited. Here, we report iron-catalyzed intermolecular [2+2] cycloaddition of unactivated alkenes and cross cycloaddition of alkenes and dienes as regio- and stereoselective routes to cyclobutanes. Through rational ligand design, development of this base metal–catalyzed method expands the chemical space accessible from abundant hydrocarbon feedstocks.

Cycloaddition reactions as exemplified by the venerable [4+2] Diels-Alder reaction are among the most powerful in organic chemistry, providing an atom-economical method for the synthesis of six-membered rings (*1*). Despite their widespred utility and applications, these reactions require the use of activated substrates and are often ineffective for unactivated alkene coupling partners. Pure hydrocarbons are the principal feedstocks of the chemical industry, serving as essential precursors to fuels, films, liquid crystal displays, materials, and medicines (*2*). Among these, ethylene and propylene are the most abundant and are produced in 130 and 85 million metric tons annually, respectively, serving principally as monomers for the multibillion-dollar polyolefins industry (*3*, *4*). Ethylene is also selectively trimerized and tetramerized on large scale rendering 1-hexene and 1-octene commodity alkenes (*5*), motivating the development of new cycloaddition methods that incorporate these fundamental industrial building blocks.

Although analogous [2+2] cycloadditions to prepare cyclobutanes are thermodynamically favorable and could be similarly transformative in synthesis, the exploration of the chemical space of four-membered carbocycles has been substantially hindered by the lack of selective methods for their synthesis (*6*). One challenge in realizing a practical method is overcoming the high kinetic barrier imparted by the thermal constraints of orbital symmetry (*7*). The use of activated alkenes (*8*) and substrates that have the appropriate redox potentials to interact with photocatalysts (*9*, *10*) have been described that overcome these challenges, and examples with high degrees of regio- and stereoselectivity have recently been reported (*11*, *12*). Unactivated alkenes, such as those available in vast excess from shale gas reserves and biorenewable sources, are currently outside the scope of these methods (*13*). Although theoretical methods predict the photochemical feasibility of such cycloadditions (*7*), photodimerization of unactivated alkenes, typically conducted in the presence of copper catalysts, is limited to selected cyclic alkenes and often yields mixtures of products, highlighting the potential utility of alternative methods for cyclobutane synthesis (*14*).

Transition metal catalysis offers the prospect of promoting the [2+2] cycloaddition of unactivated alkenes by virtue of valence d-orbitals and low-energy pathways to metallacyclic intermediates (*15*). Nickel-phosphine combinations have been reported for the synthesis of cyclobutanes from dienes and unactivated alkenes, although both yields and selectivities are not synthetically useful (*8*). Related examples with Ti, Mn, and Fe have also been described and suffer from the same limitations in yield and selectivity (*8*). Examples of more-selective alkene [2+2] cycloadditions with stoichiometric Mg, allyl chloride, and an Al reagent in the presence of Zr and Pd additives have also been reported (*16*).

Our group has found that iron and cobalt complexes bearing redox-active pyridine(diimine) ligands, which undergo reversible one-electron transfer with the transition metal, promote the intramolecular [2+2] cycloadditions of α,ω-dienes to yield the corresponding bicyclo[2.3.0]heptanes (Fig. 1A) (*17*–*19*). These base metal–catalyzed reactions proceed with unactivated dienes at ambient temperature, and mechanistic studies support reductive elimination from metallacyclic intermediates as the key C–C bond–forming step. In both iron (*18*) and cobalt (*19*) examples, the redox active pyridine(diimine) adopts its one-electron-reduced form, resulting in a more-oxidized metal center, and likely facilitates the directional, cyclobutane-forming $C(sp^3)$-$C(sp^3)$ reductive elimination.

The identification of selective, intermolecular variants of the base metal–catalyzed [2+2] cycloaddition is key to the development of a more broadly useful method compatible with abundant, unactivated alkenes. With the first-generation iron precatalyst, $(^{iPr}PDI)Fe(N_2)$ [^{iPr}PDI = 2,6-(2,6-$^{i}Pr_2$-C_6H_3-N=CMe)$_2C_5H_3N$, iPr is an isopropyl group, and Me is a methyl group], addition of common unfunctionalized terminal alkenes, such as propylene or 1-hexene, resulted in formation of a stoichiometric quantity of the corresponding alkane, arising from transfer hydrogenation from one of the isopropyl aryl groups on the iron catalyst (*20*). New approaches to catalyst design were therefore necessary to promote C–C bond formation via an iron metallacycle followed by $C(sp^3)$-$C(sp^3)$ reductive elimination. Here, we report that iron precatalysts attained through rational ligand design enable the regio- and stereochemically controlled synthesis of 1,2- and 1,3-disubstituted cyclobutanes by thermal [2+2] cycloaddition.

In an attempt to prevent transfer dehydrogenation, we synthesized an iron precatalyst lacking β-hydrogens on the aryl substituents, $[(^{Me}PDI)Fe(N_2)]_2(\mu\text{-}N_2)$], and observed catalytic turnover with propylene to produce a 2:1 mixture of 2,3-dimethylbutene and *trans*-1,2-dimethylcyclobutane. It is likely these products derive from a common iron metallacyclic intermediate, where β-hydrogen elimination followed by C-H reductive elimination yields the "tail-to-tail" dimerization product—a precursor to an

Department of Chemistry, Princeton University, Princeton, NJ 08544, USA.
*Corresponding author. E-mail: pchirik@princeton.edu

Science AAAS

Production of amorphous nanoparticles by supersonic spray-drying with a microfluidic nebulator

Esther Amstad *et al.*

Science **349**, 956 (2015);
DOI: 10.1126/science.aac9582